TWO-DIMENSIONAL HYDRODYNAMIC MODELLING OF AlGaN/GaN TRANSISTOR-BASED THz DETECTORS

J. Vyšniauskas[a], K. Ikamas[a, b], D. Vizbaras[a], and A. Lisauskas[a]

[a] *Institute of Applied Electrodynamics and Telecommunications, Vilnius University, Saulėtekio 3, 10257 Vilnius, Lithuania*
[b] *Research Group on Logistics and Defense Technology Management,*
General Jonas Žemaitis Military Academy of Lithuania, Šilo 5A, 10322 Vilnius, Lithuania
Email: alvydas.lisauskas@ff.vu.lt

Here, we report on numerical modelling of AlGaN/GaN HEMT terahertz detectors using a two-dimensional solver based on three Boltzmann transport equation (BTE) moments and the Poisson equation. We use the Synopsys TCAD Sentaurus program package, which offers a wide material database and the possibility to include traps and polarization charges for the formation of the channel without any doping. The implications of different levels of model simplifications are addressed both analytically and numerically. We calculated the current responsivity $\Re_\mathrm{I}$ to THz radiation on the drain voltage in the frequency range 0.01–3.0 THz for three AlGaN layer thicknesses d = 15, 20 and 25 nm and different gate lengths. We demonstrate that only a hydrodynamic model can reproduce the change in the sign in current responsivity at the gate voltage U_G0 ($\Re_\mathrm{I}$ = 0 at $U_\mathrm{G} = U_\mathrm{G0}$). The energy flux factor in the energy balance equation determines this effect. For the simulated structures, we find that the noise equivalent power may be as low as 0.1 pW/$\sqrt{\mathrm{Hz}}$ at 0.04 THz and 10 pW/$\sqrt{\mathrm{Hz}}$ at 3.0 THz.

Keywords: power detectors, field effect transistor (FET), gallium-nitride, terahertz (THz), hydrodynamic modelling, TCAD

1. Introduction

Since seminal papers of Dyakonov and Shur [1–3] were published, a lot of experimental work was done for the extension of signal generation and detection to the terahertz frequency band. High electron mobility transistors (HEMT) and n-type metal oxide semiconductor transistors (nMOS) are among the most popular THz detectors working at room temperature. A large variety of transistor and antenna models are used to interpret the experimental results. Antenna design and modelling is a very important part of the THz detector as well as the transistor physical model. In some cases, these two models (antenna and transistor) may be considered separately, for example, by replacing the antenna connected to the transistor electrodes with the equivalent AC voltage source. In such a case, we can investigate the transistor's DC current or voltage response to the abovementioned AC voltage source. The main goal of this investigation is to find

the connection between the internal physical processes of the transistor and the DC response. What physical processes are in consideration depends on the model of the transistor.

All models found in the literature may be divided into several groups. The models are based on the Boltzmann transport equation (BTE) moments: two moments in the drift-diffusion (DD) model, three moments in the hydrodynamic (HD) model, and even four moments in the extended hydrodynamic (EHD) one. Another group of the models is based on the stochastic or deterministic direct solving of the BTE. The stochastic model is known as the Monte Carlo (MC) procedure, in which real electrons are replaced with the so-called 'macro particles'. The deterministic BTE solvers are based on some kind of expansion of the distribution function in the Fourier series, spherical harmonic series (SHE), or Legendre polynomials. All the abovementioned models may be divided into one-dimensional (1D) or two-dimensional (2D)

ones with respect to the space dimensions in use. To our knowledge, no three-dimensional models of THz detectors exist in the literature.

Very popular 1D model [1–8] is based on the two first BTE moments: the continuity equation and the momentum balance equation (Euler equation) without pressure gradient. The Poisson equation is not included in the model. Further simplification of the Euler equation excludes time and convective derivatives from the model [4, 9–11]. Nonetheless, for the control of electron density in the transistor channel on the gate voltage, the unified charge control model (UCCM) [12–15] is used in Refs. [4, 9–11]. The main advantage of these models is their simplicity, which allows us to get analytical expressions for DC response to the incoming THz signal. In some cases [1–8], continuous or damped plasma waves may be observed. The main disadvantage of the models [1–11] is ignoring totally the 2D nature of the HEMT or nMOS transistor. The UCCM model cannot replace correctly the 2D Poisson equation, which describes electrostatic potential distribution in the transistor structure. Ignoring the diffusion term in the Euler equation may overestimate the existence of continuous plasma waves in the transistor channel. In the models under consideration, electron mobility degradation due to electron transfer to higher valleys (HEMT) or velocity saturation at a high electric field (nMOS) is not included. It is not a problem when detecting weak THz signals, but may lead to substantial errors when finding THz generation at high drain current densities (Dyakonov–Shur instabilities).

The pseudo-2D model proposed in Refs. [16, 17] is based on the continuity equation, the Euler equation with diffusion and the pseudo-2D Poisson equation. An additional term in the Poisson equation allows the control of the electron density in a gated region with respect to gate voltage. As in the UCCM case, this model simplifies the solution of equations but cannot correctly describe the two-dimensional nature of electron transport.

The semi-two-dimensional model [18] includes 1D transport (continuity and Navier–Stokes equations with diffusion and viscosity) and 2D Poisson equations. In the paper, the importance of including time and convective derivatives in the Navier–Stokes equation for searching Dyakonov–Shur instabilities is shown. Including the viscosity term, the hyperbolic Euler equation becomes the para-bolic Navier–Stokes equation, which allows the use of the efficient Scharfetter–Gummel scheme [19] to stabilize numerical calculations. Unfortunately, the effect of viscosity on the calculation results is unclear from the paper.

The 2D drift-diffusion model of nMOS was used in Ref. [20]. It includes the continuity equation, the current density (Euler) equation without a convective derivative, with and without a time derivative, and the Poisson equation. It was shown in the paper that the inclusion of the time derivative in calculations had a very small effect on current responsivity up to 10 THz due to the strong over-damping of plasma waves by the low electron momentum relaxation time in silicon.

The next step of model improvement is based on using three BTE moments. Pseudo-2D models use 1D electron transport and a more or less simplified model of electron density control by gate voltage. In one of them, the electron density in the channel is calculated by iteratively and self-consistently solving 1D Schrödinger and Poisson equations in the direction perpendicular to the charge transport direction [21]. Poisson equation in the propagation direction is also coupled to the transport equations. In the paper [21], the combined frequency- and space-domain series-expansion approach allows the avoidance of numerical instabilities and sufficiently reduces the computer simulation time of modelling systems with very long transient processes. Another approach uses UCCM for electron density control in the channel by gate voltage without solving Poisson equation in the charge transport direction [22–25]. The main feature of the model used in these papers is the temperature-dependent viscosity and heat conductivity coefficient. The proposed HD model was applied to GaAs and GaN channels. It was shown that the quality factor of plasma wave resonance decreases with the electron flow viscosity and pressure gradient. In the large signal case, shock waves may be formed in the HEMT channel [24]. InGaAs/GaAs HEMT's response to amplitude-modulated signals shows that modulation frequency may be as high as 1 THz [25].

Two-dimensional HD models may be divided into two groups. One of them consists of the pseudo-2D model [22, 23] extended to the direction perpendicular to the electron transport direction and parallel to the gate electrode plane [26–28]. This

model allows the investigation of oblique waves in wide transistors. Resonance detection depends on the transverse wave vector and drain current [27]. The response of InGaAs HEMT to the 10 fs pulse and the step function of gate voltage was investigated in Ref. [28]. In the second group of 2D models, the 2D plane is parallel to the electron transport direction and perpendicular to the gate electrode plane. Papers related to the second group [29–34] use mainly TCAD (technology computer-aided design) program packages in which 2D Poisson equation is included. Realistic structures in the non-resonant detection mode have been modelled using these packages: Si nMOS [29, 31, 34], AlGaN/GaN [30, 34], Si/SiGe [32] and AlGaAs/InGaAs [33, 34]. The absence of time and convective derivatives in the momentum balance equation (the second moment of BTE) in TCAD models restricts their usage at relatively low frequencies ($\omega\tau < 1$), where ω denotes angular frequency and τ denotes momentum relaxation time.

The complex 1D model based on four BTE moments is proposed in Ref. [35]. A small signal case was considered in the paper for comparison with a deterministic BTE solution. The comparison shows that for correct modelling of Dyakonov–Shur instabilities at high frequencies four BTE moments must be used.

More precise models use the Monte Carlo (MC) procedure [36–38] or deterministic BTE solvers [39–45]. THz generation [36] and detection [37] was obtained using the pseudo-2D MC model of GaN channel. A more realistic 2D MC model of InGaAs HEMT was used in Ref. [38], and resonant detection at 2.5 THz was obtained. Precise MC calculations require a huge amount of computer time. The MC procedure is very useful for calibrating simpler models based on BTE moments. Deterministic BTE solvers may be as precise as MC and require less computer time. Unfortunately, to the best of our knowledge, these solvers are developed only for steady state and small signal calculations. So, the investigation of THz detection using deterministic BTE solvers is now impossible.

This short review of transistor models for THz detection shows that for a more or less correct description of physical processes in the transistor channel the two-dimensional models, based on at least the first three moments of BTE and 2D

Poisson equation, must be used. Very few papers are devoted to real 2D structures of AlGaN/GaN HEMTs [30, 34]. It still needs to clarify the role of donor levels at the AlGaN and passivation layer interface to the formation of 2D electron channel and current responsivity. Spontaneous and piezoelectric polarization must be included in the model to describe the 2D electron channel formation process correctly. The dependence of current responsivity on the thickness of the AlGaN layer may be investigated correctly when using the 2D Poisson equation in the model. The well-established experimental fact of current responsivity sign change with gate voltage [7] is not explained at this time. Also, the effect of the energy balance equation in the model on current responsivity and NEP (noise equivalent power) at different THz frequencies needs to be clarified. Our paper is devoted to solving the abovementioned problems using the Synopsys TCAD Sentaurus program package.

The paper is divided into three parts. In Section 2, the analytical approach using simplified analytical equations for the description of high-frequency transport is discussed. Five different assumptions of a one-dimensional analytical hydrodynamic transport model are presented. Section 3 presents the AlGaN/GaN HEMT terahertz detector model and calculation methodology in the TCAD environment. Section 4 is dedicated to the modelling results.

2. Simplified hydrodynamic equations

Before proceeding with numerical calculations, we would like to give a special analysis related to high-frequency transport using a one-dimensional analytical hydrodynamic transport model.

According to the approach proposed by Dyakonov and Shur [2], the basis of the model is defined by the solution of balance equations. The equation of motion with respect to the electron velocity v is

$$\frac{\partial v}{\partial t} + v\frac{\partial v}{\partial x} - \frac{q}{m^*}E - \frac{k_B}{m^*}\frac{\partial nT}{\partial x} + \frac{v}{\tau_p} = 0, \qquad (1)$$

where n is the carrier density, q and m^* are the electron charge and effective mass, E is the electric field, τ_p is the momentum relaxation time, k_B is the Boltzmann constant, and T is the temperature. Here, we keep the so-called pressure term, often omitted when analyzing plasmonic excitations. This

221 ISSN 1648-8504 eISSN 2424-3647

J. Vyšniauskas et al. / Lith. J. Phys. **63**, 218–232 (2023)

equation should be solved together with the charge continuity equation

$$\frac{\partial n}{\partial t} + \frac{\partial nv}{\partial x} = 0. \tag{2}$$

The depth of analysis can be extended by considering the inhomogeneous heating of charge carriers from the solution of the energy balance equation

$$\frac{\partial \xi}{\partial t} + v\frac{\partial \xi}{\partial x} - qvE + \frac{k_B}{n}\frac{\partial nvT}{\partial x} + \frac{\xi - \xi_0}{\tau_e} = 0, \tag{3}$$

where $\xi = (m^* v^2)/2 + k_B T$ is the electron energy consisting of kinetic and thermal (here, a pre-factor 1 in front of the temperature term accounts for a two-dimensional nature of the transistor channel) components. τ_e is the energy relaxation time, and ξ_0 is the equilibrium electron energy $k_B T_0$ corresponding to the lattice temperature T_0. The energy conservation equation Eq. 3 assumes a displaced Maxwellian distribution, with higher-order moments of distribution function diminishing. Therefore, the heat flow due to the electron gas (the third moment of the distribution function) is not considered. One must note that most device-simulating methods use an equation set for the current density J_n rather than velocity v. There is a straightforward way to rewrite the equations by applying the definition $J_n = qnv$ and invoking the continuity equation; however, in this section, we will remain with the representation originally proposed in Ref. [2].

In order to find analytical solutions, it is accustomed to apply harmonic analysis and, assuming that the absolute values of oscillating carrier density $n_1 e^{-i\omega t}$ and electron temperature $T_1 e^{-i\omega t}$ terms are much smaller than the stationary quantities n_0 and T_0, to linearize the system of partial differential equations. These assumptions simplify the energy balance equation to

$$-i\omega T_1 + k_B T_0 \frac{dv_1}{dx} + \frac{T_1}{\tau_e} = 0, \tag{4}$$

where v_1 is the oscillating velocity term. Equation 4 allows us to relate oscillating electronic temperature with the gradient of oscillating velocity, i.e.

$$T_1 = \frac{T_0 \tau_e}{i\omega\tau_e - 1}\frac{dv_1}{dx}. \tag{5}$$

The continuity equation under the assumption of harmonic excitation is as follows:

$$-i\omega n_1 + n_0 \frac{dv_1}{dx} = 0. \tag{6}$$

Similarly, the equation of motion can be expressed in the following form:

$$-i\omega v_1 - qE_1 - \frac{k_B T_0}{n_0}\frac{dn_1}{dx} - k_B \frac{dT_1}{dx} + \frac{v_1}{\tau_p} = 0. \tag{7}$$

The simple form of the solution of the system of Eqs. 4, 6 and 7 can be obtained by making additional conveniently used assumptions: by relating the local potential ϕ_1 and concomitant $E_1 = -d\phi_1/dx$ with the carrier density n_1, i.e. setting the functional relation $n_1 = f(\phi_1)$. Now, having a simple system with three equations and three unknowns v_1, n_1 (or rather potential ϕ_1) and T_1 one can rearrange them to obtain a simple expression of the wave equation for the velocity,

$$\frac{\partial^2 v_1}{\partial x^2} + k^2 v_1 = 0, \tag{8}$$

where k is the wavenumber. Depending on the initial assumptions or the level of truncation of hydrodynamic analysis, k might obtain different forms, which are summarized in Table 1. Here s is defined as

$$s = \sqrt{\frac{q}{m^*} n_0 \frac{dV_G}{dn}}, \tag{9}$$

with V_G being the gate voltage and dn/dV_G representing the change of carrier density on gate voltage change.

In order to find an explicit solution of Eq. 8, one has to apply appropriate (adequate for the experimental implementation) boundary conditions. Often, it is assumed that the gate-to-source potential oscillations at the beginning of the channel oscillate with the amplitude of the applied voltage oscillations, i.e. $\phi_1(0) = u_a$ and there is no current flowing through the drain terminal or $v_1(L) = 0$. Under these assumptions, one can easily arrive at the impedance of the device which is relevant for the antenna:

$$Z = \frac{ikm^* s^2 \cot(Lk)}{W \omega q^2 n_0}, \tag{10}$$

where L and W are the gate length and width of the transistor. The analytical method can be further extended to account for rectification; however, this

gets out of the scope of this manuscript. Nevertheless, we want to address several important aspects which directly emerge from this analysis on the analytical level.

Table 1. A summary of solutions for the wavenumber k using different model assumptions.

Conditions	Wavenumber k
Distributed RC	$\sqrt{\dfrac{i\omega}{s^2\tau_p}}$
Without energy balance, no diffusion	$\sqrt{\dfrac{\omega(i+\omega\tau_p)}{s^2\tau_p}}$
Without energy balance, with diffusion	$\sqrt{\dfrac{\omega(i+\omega\tau_p)}{s^2\tau_p - \dfrac{T_0 k_B \tau_p}{m^*}}}$
With energy balance, no diffusion	$\sqrt{\dfrac{\omega(i+\omega\tau_p)}{s^2\tau_p - \dfrac{T_0 k_B \omega \tau_p \tau_e}{m^*(i+\omega\tau_e)}}}$
Full solution	$\sqrt{\dfrac{\omega(i+\omega\tau_p)}{s^2\tau_p - \dfrac{T_0 k_B \tau_p(i+2\omega\tau_e)}{m^*(i+\omega\tau_e)}}}$

Typically, the diffusion and energy terms in balance equations are treated as negligible and often omitted for analytical modelling. While omitting these terms does not change the form of the solution, the k and, in turn, Z can change quite drastically depending on the system parameters. In Fig. 1, we show the difference between the real and imaginary parts of the impedance spectrum. The operating parameters are arbitrarily selected but are close to those of a realistic GaN transistor (with L = 250 nm and W = 1 μm) in the sub-threshold gate bias conditions. Hydrodynamic equation solutions are visualized by taking all terms or omitting different components. The reference case (a red solid line) is the classical solution [2] without diffusion or energy terms and demonstrates a gradual transition from stationary impedance to the so-called plasmonic waveguide, which shows a characteristic real part of impedance with a diminishing imaginary part. The distributed RC model equivalent omits the derivative of velocity in the equation of motion (a black line). It is followed by solutions with these terms added explicitly (green and blue lines) and, finally, a solution of all terms included (a magenta line).

It should be noted that considering the diffusion near the threshold voltage is also important for the stationary conductivity of the channel, which is represented by a lower value of the resulting resistance. Furthermore, we observe a continuous decrease in the real part of channel impedance for all situations except for the reference case. Implications can be elucidated even further by analyzing the imaginary part of impedance presented at the right panel of Fig. 1, demonstrating that it saturates at a specific value. Therefore, we can summarize that, just by adding the diffusion and/or energy terms
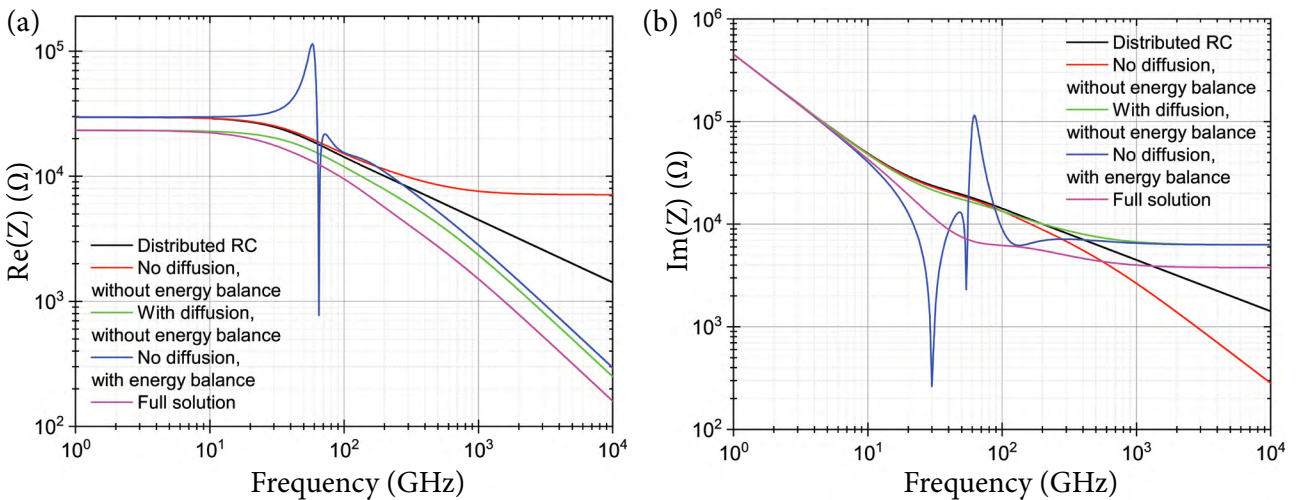
Fig. 1. Comparison between the real and imaginary parts of transistor impedance vs. frequency when different terms of the hydrodynamic charge transfer equation are omitted.

223 ISSN 1648-8504 eISSN 2424-3647

J. Vyšniauskas et al. / Lith. J. Phys. **63**, 218–232 (2023)

to the hydrodynamic equation, we expect to observe a decrease in the real part of impedance, which becomes closer to a full solution by omitting the time derivative of velocity but including diffusion terms and considering the energy balance equation rather than solving only the transport equation with neglected diffusion and energy balance. Furthermore, in real structures, the electronic temperature in the ungated region is expected to be different from the gated part, which can result in the build-up of an additional potential that cannot be taken into account by the simplified analytical theory. Therefore, in the following sections, we will concentrate on a thorough numerical modelling of THz rectification in realistic AlGaN/GaN HEMT structures.

3. AlGaN/GaN HEMT terahertz detector TCAD model and calculation methodology

The numerically modelled HEMT structure consists of an undoped $Al_{0.2}Ga_{0.8}N$ layer, an undoped 500 nm GaN layer, a 25 nm Si_3N_4 passivation layer and a 5 nm SiO_2 substrate (the last one not shown in Fig. 2). The main part of the results in the 0.01–3 THz frequency band was obtained using the dimensions of gated (L_G) and ungated (L_{SG}, L_{GD}) regions shown in Fig. 2 and the first row of Table 2 for three values of AlGaN layer thickness d = 15, 20 and 25 nm. For comparison, some calculations were made using L_G = 100, 300 and 900 nm with $L_{SG} = L_{GD}$ = 100 nm at 1 THz. At the $Si_3N_4/Al_{0.2}Ga_{0.8}N$ interface, we included a deep level of donors located at 0.4 eV from the middle of the band gap. The donor density was changed from zero to 5×10^{13} cm^{-2}.
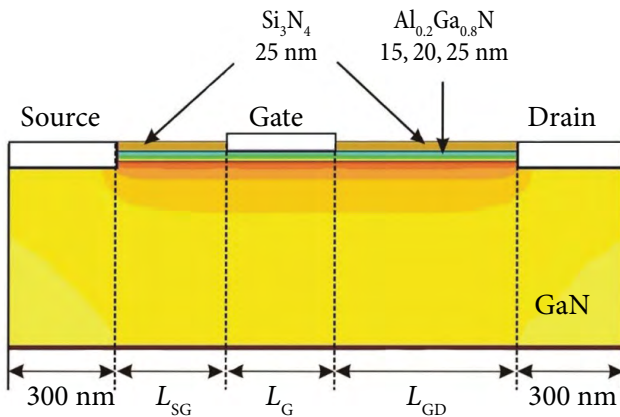
Fig. 2. The structure of AlGaN/GaN HEMT employed for the numerical simulations of THz detection.

Table 2. Dimensions of gated and ungated regions in Fig. 2.

	L_{SG}, nm	L_G, nm	L_{GD}, nm
1	300	300	500
2	100	300	100
3	100	100	100
4	100	900	100

Spontaneous polarization and piezoelectric charges were included in the model for the formation of the 2D electron channel. The carrier mobility dependence on the doping density and carrier temperature was considered. The Shockley–Read–Hall (SRH) and Auger recombination were included in the model. All numerical simulations are performed in 2D assuming homogeneous properties in the lateral dimension assumed to be 1 μm.

All numerical calculations were made using the Synopsys TCAD Sentaurus program package. The set of 2D differential equations consists of three BTE moment equations: the continuity equation, the current density equation and the energy balance equation for electrons and holes, which are complemented with the Poisson equation. Let us address these equations in detail. The Poisson equation is

$$\nabla \cdot (\varepsilon \nabla \phi + \mathbf{P}) = -q(p - n + N_D - N_A) - \rho_{trap}, \quad (11)$$

where ε is the dielectric permittivity of the material, $\mathbf{P}$ is the ferroelectric polarization vector, ρ_{trap} is the charge density contributed by traps and fixed charges. ϕ is the electrostatic potential, n and p are the electron and hole density, N_D and N_A are the donor and acceptor density, and q is the elementary electronic charge.

The continuity equation for electrons is as follows:

$$q \frac{\partial n}{\partial t} - \nabla \cdot \mathbf{J}_n = -qR_{net,n}, \quad (12)$$

where $R_{net,n}$ is the electron net recombination rate. The electron current density vector equation is

$$\mathbf{J}_n = \mu_n \left(n\nabla E_C + k_B T_n \nabla n - nk_B T_n \nabla \ln(\frac{n}{N_C}\exp(-\eta_n)) \right.$$
$$\left. + f_{TDn} \frac{F_{1/2}(\eta_n)}{F_{-1/2}(\eta_n)} k_B n \nabla T_n \right), \quad (13)$$

$$\eta_n = \frac{E_{\mathrm{F},n} - E_\mathrm{C}}{k_\mathrm{B}T}, \tag{14}$$

where μ_n is the electron mobility, E_C is the conduction band energy, k_B is the Boltzmann constant, T_n is the electron temperature, T is the lattice temperature, N_C is the effective density of states, $E_{\mathrm{F}n}$ is the quasi-Fermi energy for electrons, $f_{\mathrm{TD}n}$ is the thermo diffusion factor, $F_{1/2}$ and $F_{-1/2}$ are the Fermi integrals of 1/2 and –1/2 order. Due to a possible very high electron density in the channel, Fermi–Dirac statistics were used. Compared with the full hydrodynamic description, the current density equation lacks two terms: the time derivative of current density as well as the convective term. However, as has been addressed earlier in the analytical section, the transport description does not deviate until about 1.4 THz at which $\omega\tau_p = 1$. The electron energy balance equation is as follows:

$$\frac{\partial W_n}{\partial t} + \nabla \cdot \mathbf{S}_n = \frac{\mathbf{J}_n \cdot \nabla E_\mathrm{C}}{q} - H_n - \xi_n \frac{W_n - W_{n0}}{\tau_{\mathrm{en}}}, \tag{15}$$

$$W_n = n \frac{3 k_\mathrm{B} T_n}{2}, \tag{16}$$

$$\mathbf{S}_n = \frac{5}{2} R_n \frac{F_{1/2}(\eta_n)}{F_{-1/2}(\eta_n)}$$
$$\times \left(\frac{k_\mathrm{B} T_n}{q} \mathbf{J}_n + f_{\mathrm{HC}n} \frac{k_\mathrm{B}^2}{q} n \mu_n T_n \nabla T_n \right), \tag{17}$$

where H_n is the energy gain/loss term due to generation–recombination processes, the parameter ξ_n improves numeric stability – speeds up relaxation for small densities and approaches 1 for large densities, W_{n0} is the the energy density at $T_n = T_p = T$, τ_{en} is the electron energy relaxation time, $\mathbf{S}_n$ is the electron energy flux vector, R_n is the electron energy flux factor, and $f_{\mathrm{HC}n}$ is the heat conductivity factor. In this approximation, the electron energy is defined only by the thermal energy which is a good assumption when there is no stationary bias applied between the source and drain terminals.

Similar equations as (12–17) were used for holes. It is important to note that the model must consider holes to obtain correct calculation results.

Source and drain contacts are assumed to be ohmic, whereas the gate contact is Schottky with gold as a metal. Charge neutrality and equilibrium are assumed at ohmic contacts. For Fermi–Dirac statistics, Synopsys TCAD numerically computes the equilibrium solution for electron and hole concentration. For the carrier temperatures, T_n and T_p, the fast relaxation to the lattice temperature (boundary condition $T_n = T_p = T$) is assumed at the thermal contacts. For other boundaries, adiabatic conditions for carrier temperatures are assumed. Dirichlet boundary conditions for the Poisson equation at contacts are used. Outer boundaries of the device that are not contacts are treated with ideal Neumann boundary conditions.

The parameters of all materials used in the model are obtained directly from the Synopsys material database. The electron energy relaxation time $\tau_\mathrm{e} = 0.2$ ps. The electron effective mass $m^* = 0.2\, m_0$, where m_0 denotes the free electron mass. For the moderate electron mobility $\mu_n = 1000$ cm²/Vs, the electron momentum relaxation time $\tau_p = 0.11$ ps. From the inequality $\omega\tau_p < 1$, we have the upper frequency of confidence $f = 1.4$ THz for our model due to the absence of time and convective derivatives in the current density equation, which will be presented later in the manuscript.

For the investigation of THz detection, we used a simple circuit with DC voltage supply U_G connected to the transistor gate and source, and THz AC voltage supply V_AC connected to the transistor drain and source. The detected signal equals the DC component I_DC of drain current. The current responsivity $\Re_I = I_\mathrm{DC}/P_\mathrm{AC}$, where P_AC denotes THz power absorbed by the transistor. Therefore, the simulated responsivity refers to the electrical performance of the device, whereas for the estimation of optical performance, one has to account for the efficiency of the antenna, impedance matching, etc. We used the V_AC amplitude equal to 50 mV. It is worth to note that I_DC comprises a very small part of the drain current amplitude (0.01 or less). In such a case, special requirements must be fulfilled for calculating I_DC. We integrated exactly over one period of drain current oscillations at the end of transient processes, after which the strong periodicity of oscillations was achieved. The time step during calculation is defined by the program in order to avoid numerical instabilities. In addition, we limit the time step to some maximal value for obtaining at least 100 time points during one period of oscillations. The channel impedance and drain current harmonics were calculated using the standard Fast Fourier Transform (FFT).

4. The modelling results

This section presents the numerical modelling results. Three major aspects of the HEMT-based detector structure and performance are addressed. For the first, we will investigate the effect of donor density in the AlGaN/SiN interface. Then, the static channel resistance and impedance calculation results will be presented. In the last part, we will estimate the main performance characteristics of the detector – current responsivity and noise equivalent power.

4.1. The effect of donor density in the AlGaN/SiN interface

We investigated the dependence of electron density in the ungated areas of the HEMT channel on the donor density N_D in the AlGaN/SiN interface. These areas are passive and create additional losses when a transistor works as a terahertz radiation detector. Lowering the N_D lowers the electron density in the ungated areas of the channel. As a result, the detector sensitivity decreases. Another important fact must be taken into consideration. There are always negative polarization charges near the AlGaN/SiN interface, and these charges attract holes. It creates a high-density hole channel that distorts the static and dynamic characteristics of the transistor. The electrons from the donor level penetrate the 2D channel in the ungated areas, the rest of the ionized donors partially or fully compensate for the negative polarization charge, and the hole channel is not

formed. Figure 3(a) presents an electron density distribution in the 2D channel at different N_D densities. When N_D is changed from 0 to $5 \cdot 10^{13}$ cm^{-2}, the electron density in the ungated areas changes about seven times. $N_D = 5 \cdot 10^{13}$ cm^{-2} is an optimal choice because it fully compensates for the polarization charge and ensures a high density ($4 \cdot 10^{19}$ cm^{-3}) in the ungated areas. Due to this reason, practically all further calculations were made using $N_D = 5 \cdot 10^{13}$ cm^{-2}.

For comparison, several calculations were performed using $N_D = 2.3 \cdot 10^{13}$ cm^{-2}. Figure 3(b) presents the distribution of electron density in the channel versus DC drain voltage U_D when $U_G = 0$ and $N_D = 2.3 \cdot 10^{13}$ cm^{-2}.

By increasing the drain voltage, the electron density along the channel starts to decrease enabling the so-called resistive mixing which can be utilized for detection.

4.2. Static resistance and impedance

Static resistance of the channel and the impedance of the transistor were calculated for the three values of AlGaN layer thickness: $d = 15$, 20 and 25 nm. The static resistance (Fig. 4) is one of the main parameters for calculating the noise equivalent power. Threshold voltage strongly depends on the AlGaN layer thickness. The impedance of the transistor (Fig. 5) depends on the gate voltage and frequency. The real part of the impedance has the maximum at the gate voltage slightly higher than the threshold voltage. At low frequencies $f \leq 0.1$ THz, the real
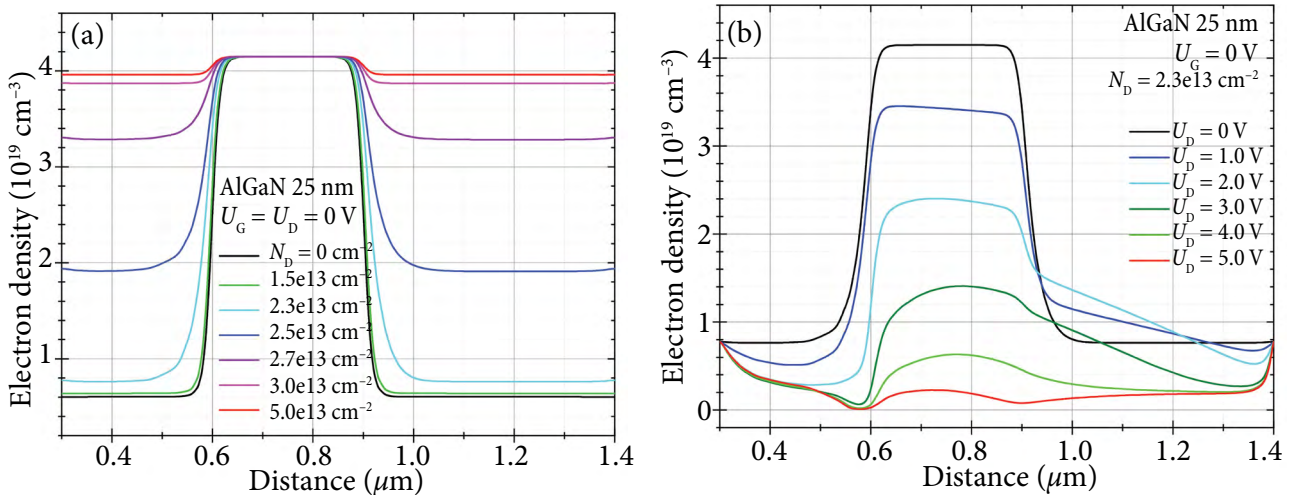
Fig. 3. (a) The electron density distribution in the channel at the equilibrium versus different donor densities in the AlGaN/SiN interface. (b) The electron density distribution in the channel versus drain voltage when the donor density is lower than optimal.
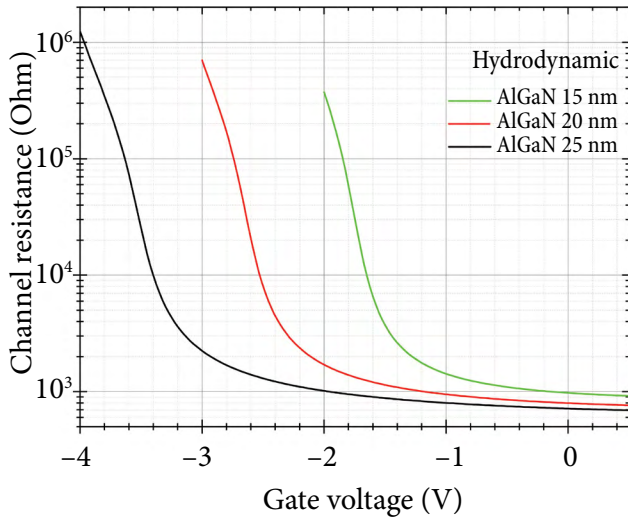
Fig. 4. Channel static resistance versus gate voltage at three values of AlGaN layer thickness.

part approaches the static resistance with gate voltage increase. At higher frequencies, the real part is sufficiently lower than the static resistance. The imaginary part of the impedance has a capacitive nature and increases monotonically with the gate voltage. The knowledge of the impedance is very important when constructing the antenna for the optimum power delivery from the antenna to the transistor.

4.3. Current responsivity and noise equivalent power

The electrical current responsivity $\mathfrak{R}_I$ was calculated using the hydrodynamic (HD) and drift-diffusion (DD) models for the three abovementioned values of parameter d, $L_G = 300$ nm, $L_{SG} = 300$ nm and
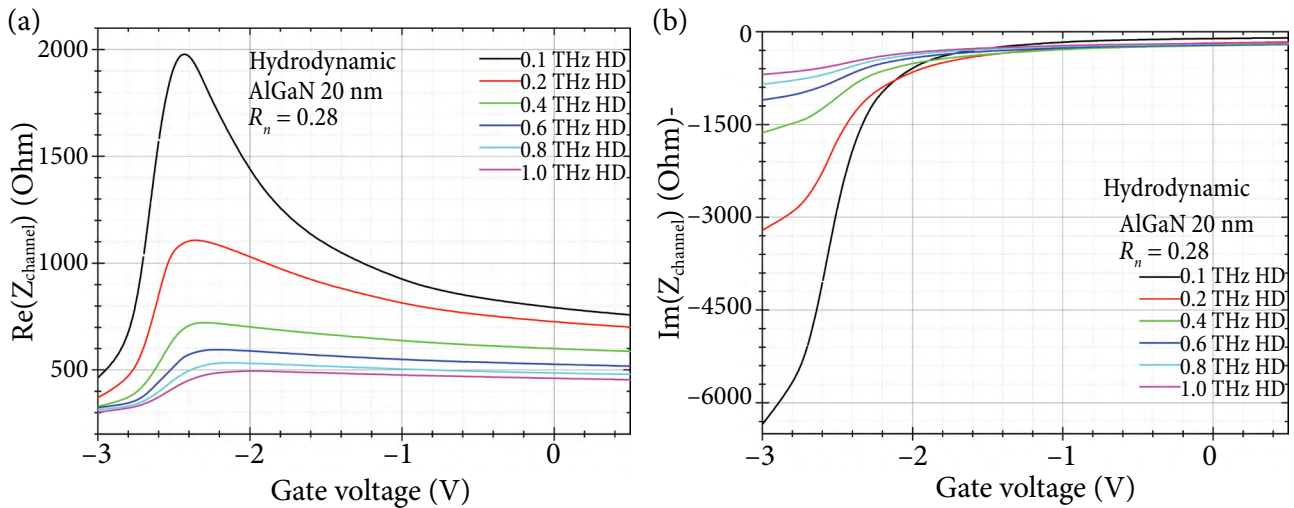
Fig. 5. Real and imaginary parts of the transistor impedance versus gate voltage at different frequencies.
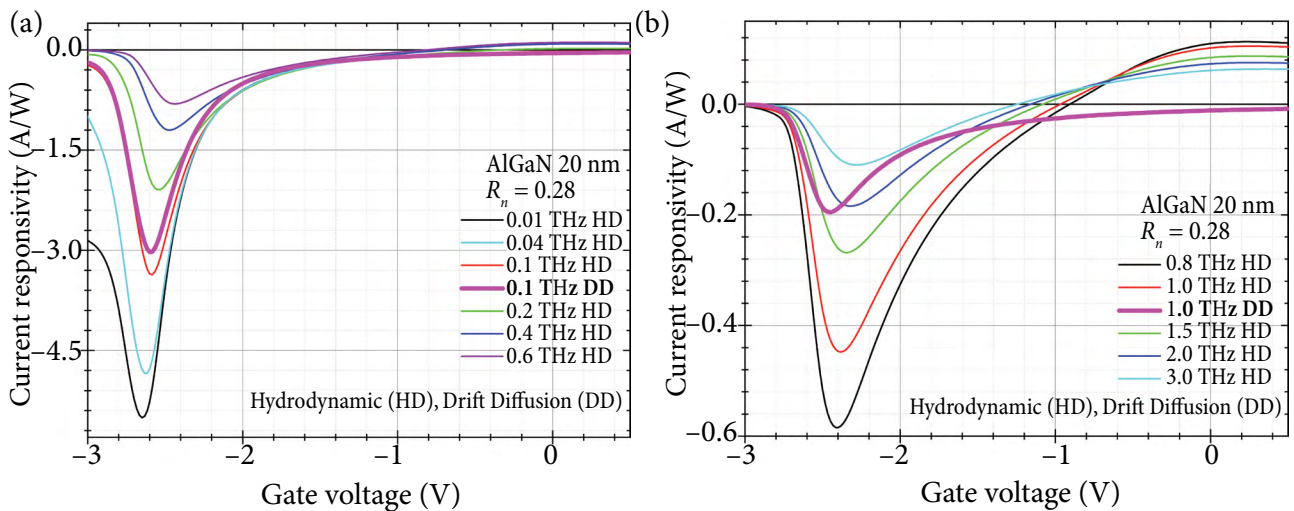
Fig. 6. Current responsivity versus gate voltage at different frequencies for the device with a 20 nm-thick AlGaN layer. The drift diffusion model (DD) case is highlighted.

L_{GD} = 500 nm. The results for d = 20 nm are shown in Fig. 6. Similar results were obtained also for another two values of d. The $\Re_I$ maximum is almost the same for all three cases of d. The maximum of electrical responsivity as a function on the frequency at d = 15 and 20 nm is shown in Fig. 7(a). Gate voltage at the $\Re_I$ maximum differs significantly due to the difference of the threshold voltage (U_{th} = –1.8 V at d = 15 nm, –2.8 V at d = 20 nm and 3.6 V at d = 25 nm). The NEP dependence on the gate voltage at different frequencies is shown in Fig. 7(b).

The main features of the current responsivity and NEP curves are the following:

(i) The highest value of current responsivity is at the gate voltage slightly higher than the threshold voltage U_{th}.

(ii) While increasing the frequency, the current responsivity decreases, but its maximum moves to the higher area of the gate voltage (see Fig. 6).

(iii) The HD and DD models show almost the same results in the low-frequency range (f = 0.01–0.1 THz). Thus, there is no need to use a more complex HD model in this frequency range. The mismatch between the HD and DD models increases while increasing frequency (Fig. 7(a)). In Figure 6(b), near 1 THz, the DD model gives 2.5 times lower current responsivity maximum at lower gate voltage.

(iv) In the case of the HD model, the current responsivity changes its sign at the gate voltage U_{G0} ($\Re_I$ = 0 at $U_G = U_{G0}$). U_{G0} decreases with the frequency increase (Fig. 6(b)). When

the coupling direction of the three-terminal-based detector is not well defined, one can obtain a reversal of the rectified current sign just from the coupling conditions [46, 47]. However, the change of the current responsivity sign for well-defined boundary conditions antenna-coupled detectors, which is of relevance for our modelling, was also experimentally demonstrated [7]. Within the assumptions of the DD model, no changes in the sign can be simulated.

(v) As a result, we can say that an HD model is necessary for relatively high frequencies. The energy balance equation (15) in the HD model takes into account thermodiffusion and electron energy transfer, which plays an important role in the detection of THz radiation with AlGaN/GaN HEMT transistors.

(vi) The minimum value of the electrical NEP is at the gate voltage slightly lower than the threshold voltage U_{th}. The NEP minimum changes from about $0.1\,\mathrm{pW}/\sqrt{\mathrm{Hz}}$ at 0.04 THz to $10\,\mathrm{pW}/\sqrt{\mathrm{Hz}}$ at 3.0 THz (Fig. 7(b)). If one accounts for optical coupling loss, these values agree well with recent findings [48–50].

There are few control parameters in the HD model, allowing one to make similarity between the calculation results and experimental findings. These parameters are f_{TDn} that controls the electron thermodiffusion coefficient, f_{TCn} that changes a value of thermal conductivity in energy flux, and R_n that regulates the total electron energy flux. It was established that the first two coefficients
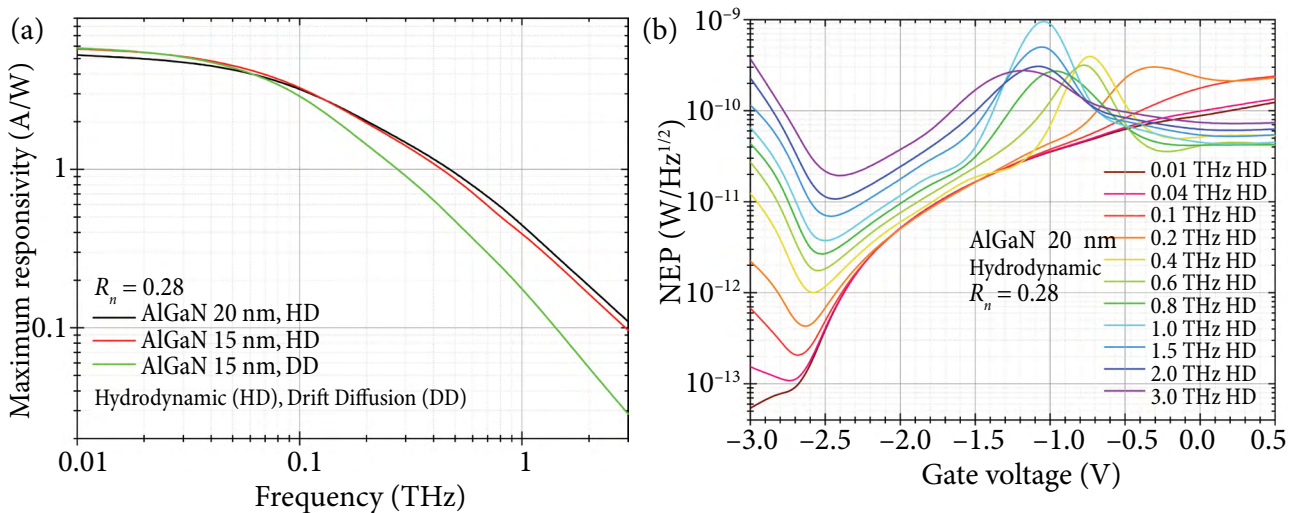
Fig. 7. (a) The maximum responsivity dependence on the frequency at different AlGaN layer thickness. (b) The noise equivalent power in the HEMT with d = 20 nm.
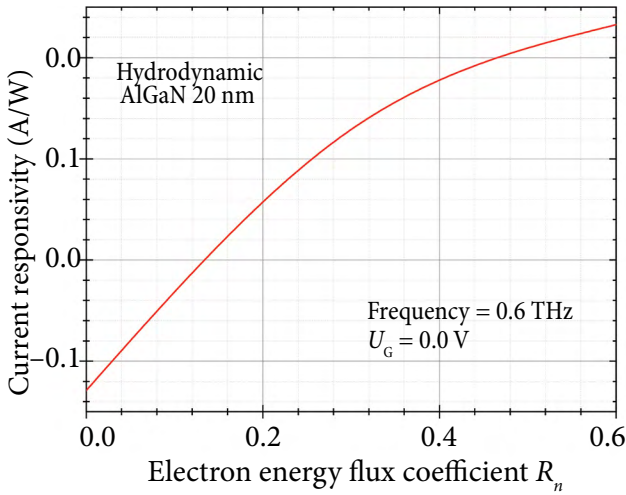
Fig. 8. The current responsivity versus electron energy flux factor at 0.6 THz and $U_G = 0$.

influence the current responsivity level just by a few percent when changing f_{TDn} and f_{TCn} from 0 to 1. By changing R_n, we obtain changes not only in the absolute value of current responsivity, but it controls even the direction of rectified current – a phenomenon that appears at high frequencies and for the above threshold gate voltage values. Figure 8 shows the current responsivity dependence on the R_n coefficient when the frequency is 0.6 THz and $U_G = 0$. For all our calculations, the following values were used: $f_{TDn} = 1$, $f_{TCn} = 1$, $R_n = 0.28$.

As shown above, the current responsivity maximum does not depend on the AlGaN layer thickness d. This result remains the same when narrowing the ungated regions to 100 nm (Fig. 9(a)).
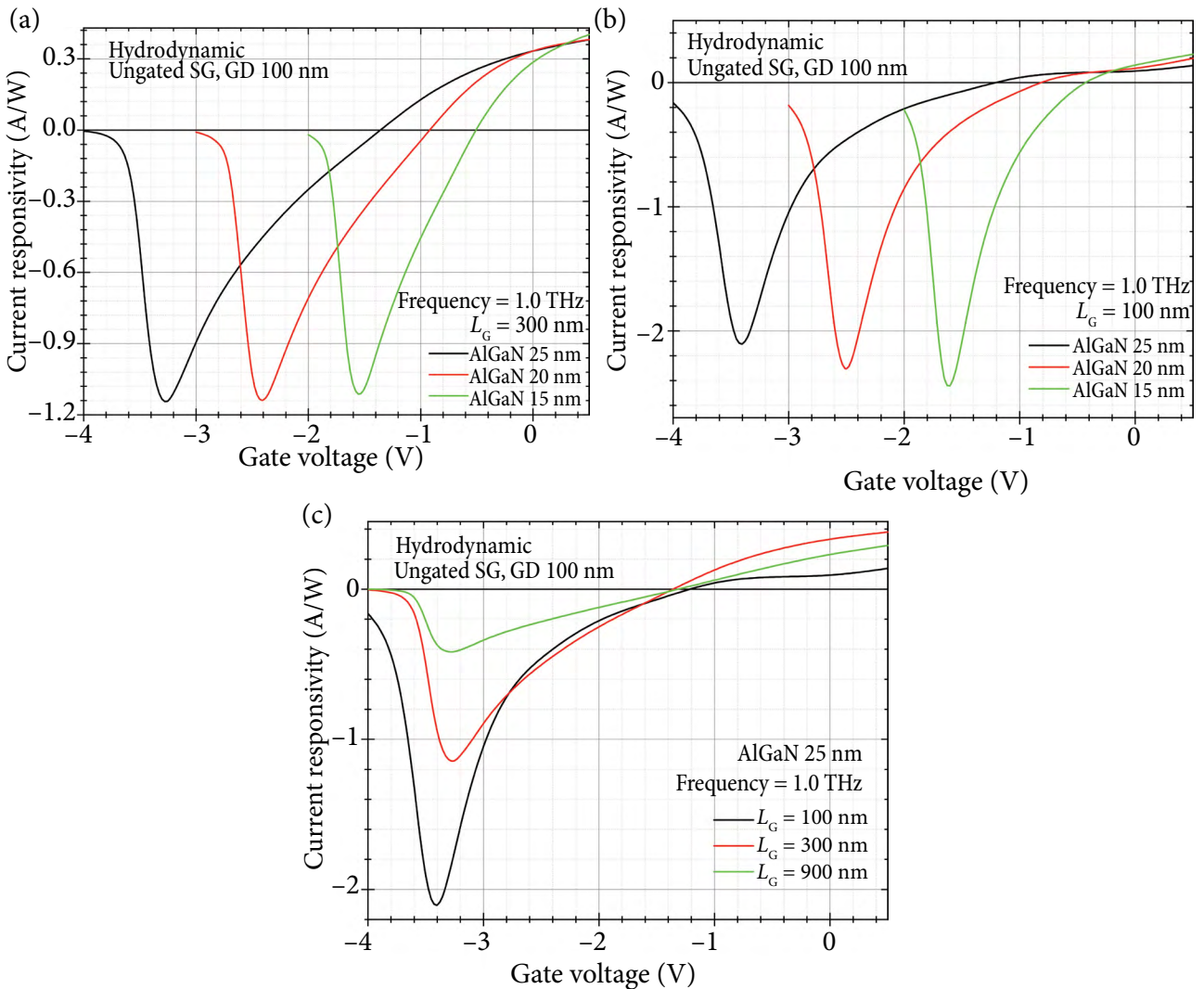
Fig. 9. (a) The current responsivity versus gate voltage at 1 THz. $L_{SG} = L_{GD} = 100$ nm, $L_G = 300$ nm. (b) The current responsivity versus gate voltage at 1 THz. $L_{SG} = L_{GD} = L_G = 100$ nm, $d = 25$ nm. (c) The current responsivity versus gate voltage at 1 THz and different $L_G = 100$ nm, 300 nm, 900 nm. $L_{SG} = L_{GD} = 100$ nm, $d = 25$ nm.

Nevertheless, the situation changes when narrowing the gate length L_G to 100 nm (Fig. 9(b)). The current responsivity increases with d decrease. The current responsivity maximum decreases significantly with gate length increase (Fig. 9(c)).

5. Conclusions

Here, we present a comprehensive review of the numerical modelling of transistor-based THz detectors. We use the analytical analysis of hydrodynamic equations and demonstrate that even a strong simplification of the transport equation allows us to address the question of collective excitations and, therefore, can be successfully applied in numerically-based solvers. We have applied a two-dimensional model based on three BTE moments, and the Poisson equation realized in the Synopsys TCAD Sentaurus program package. We find that for realistic device implementations in the AlGaN/GaN material system, the highest value of current responsivity can be obtained in the vicinity of the threshold voltage U_{th}. While increasing the frequency, the current responsivity decreases, but its maximum shifts to larger gate voltage values.

We also demonstrate that the HD and DD models show almost the same results in the low-frequency range (f = 0.01–0.1 THz). However, the mismatch between the HD and DD models increases while increasing frequency.

In the case of the HD model, the current responsivity changes its sign at the gate voltage U_{G0} ($\Re_I = 0$ at $U_G = U_{G0}$) – this effect cannot be simulated in DD. The change of the current responsivity sign coincides very well with the experimental results published in Ref. [7] and is determined by the energy flux factor in the energy balance equation.

The simulations result in the state-of-the-art noise equivalent power values, which might be as low as $0.1\,\mathrm{pW}/\sqrt{\mathrm{Hz}}$ at 0.04 THz and $10\,\mathrm{pW}/\sqrt{\mathrm{Hz}}$ at 3.0 THz. The performance of devices improves by shortening the gate length and minimizing the gate-to-channel separation.

Acknowledgements

References

[1] M. Dyakonov and M. Shur, Shallow water analogy for a ballistic field effect transistor: New mechanism of plasma wave generation by dc current, Phys. Rev. Lett. **71**(15), 2465–2468 (1993), https://doi.org/10.1103/PhysRevLett.71.2465

[2] M. Dyakonov and M. Shur, Detection, mixing, and frequency multiplication of terahertz radiation by two-dimensional electronic fluid, IEEE Trans. Electron Dev. **43**(3), 380–387 (1996), https://doi.org/10.1109/16.485650

[3] M. Dyakonov and M. Shur, Plasma wave electronics: novel terahertz devices using two dimensional electron fluid, IEEE Trans. Electron Dev. **43**(10), 1640–1645 (1996), https://doi.org/10.1109/16.536809

[4] A. Lisauskas, U. Pfeiffer, E. Öjefors, P. Haring Bolìvar, D. Glaab, and H.G. Roskos, Rational design of high-responsivity detectors of terahertz radiation based on distributed self-mixing in silicon field-effect transistors, J. Appl. Phys. **105**(11), 114511 (2009), https://doi.org/10.1063/1.3140611

[5] S. Boppel, A. Lisauskas, M. Mundt, D. Seliuta, L. Minkevičius, I. Kašalynas, G. Valušis, M. Mittendorff, S. Winnerl, V. Krozer, and H.G. Roskos, CMOS integrated antenna-coupled field-effect transistors for the detection of radiation from 0.2 to 4.3 THz, IEEE Trans. Microwave Theory Tech. **60**(12), 3834–3843 (2012), https://doi.org/10.1109/TMTT.2012.2221732

[6] M. Bauer, A. Rämer, S. Boppel, S. Chevtchenko, A. Lisauskas, W. Heinrich, V. Krozer, and H.G. Roskos, High-sensitivity wideband THz detectors based on GaN HEMTs with integrated bow-tie antennas, in: *Proceedings of the 10th European Microwave Integrated Circuits Conference (EuMIC)* (IEEE, Paris, 2015) pp. 1–4, https://doi.org/10.1109/EuMIC.2015.7345053

[7] A. Lisauskas, M. Bauer, A. Rämer, K. Ikamas, J. Matukas, S. Chevtchenko, W. Heinrich, V. Krozer, and H.G. Roskos, Terahertz rectification by plasmons and hot carriers in gated 2D electron gases, in: *Proceedings of the 41st International Conference on Noise and Fluctuations (ICNF)* (IEEE, 2015) pp. 1–5, https://doi.org/10.1109/ICNF.2015.7288628

[8] J.Y. Park, S.-H. Kim, S.-M. Hong, and K.R. Kim, Physical analysis and design of resonant plasma-wave transistors for terahertz emitters, IEEE Trans. Terahertz Sci. Technol. **5**(2), 244–250 (2015), https://doi.org/10.1109/TTHZ.2015.2392630

[9] W. Knap, V. Kachorovskii, Y. Deng, S. Rumyantsev, J.-Q. Lü, R. Gaska, M.S. Shur, G. Simin, X. Hu, M.A. Khan, C.A. Saylor, and L.C. Brunel, Nonresonant detection of terahertz radiation in field effect transistors, J. Appl. Phys. **91**(11), 9346–9353 (2002), https://doi.org/10.1063/1.1468257

[10] V. Kachorovskii and M. Shur, Field effect transistor as ultrafast detector of modulated terahertz radiation, Solid State Electron. **52**(2), 182–185 (2008), https://doi.org/10.1016/j.sse.2007.08.002

[11] A. Gutin, V. Kachorovskii, A. Muraviev, and M. Shur, Plasmonic terahertz detector response at high intensities, J. Appl. Phys. **112**(1), 014508 (2012), https://doi.org/10.1063/1.4732138

[12] Y. Byun, K. Lee, and M. Shur, Unified charge control model and subthreshold current in heterostructure field-effect transistors, IEEE Electron Device Lett. **11**(1), 50–53 (1990), https://doi.org/10.1109/55.46928

[13] C.-K. Park, C.-Y. Lee, K. Lee, B.-J. Moon, Y.H. Byun, and M. Shur, A unified current-voltage model for long-channel nMOSFETs, IEEE Trans. Electron Dev. **38**(2), 399–406 (1991), https://doi.org/10.1109/16.69923

[14] B. Moon, C. Park, K. Rho, K. Lee, M. Shur, and T. Fjeldly, Analytical model for p-channel MOSFETs, IEEE Trans. Electron Dev. **38**(12), 2632–2646 (1991), https://doi.org/10.1109/16.158685

[15] M. Shur, T.A. Fjeldly, T. Ytterdal, and K. Lee, Unified MOSFET model, Solid State Electron. **35**(12), 1795–1802 (1992), https://doi.org/10.1016/0038-1101(92)90263-C

[16] P. Nouvel, H. Marinchio, J. Torres, C. Palermo, D. Gasquet, L. Chusseau, L. Varani, P. Shiktorov, E. Starikov, and V. Gružinskis, Terahertz spectroscopy of plasma waves in high electron mobility transistors, J. Appl. Phys. **106**(1), 013717 (2009), https://doi.org/10.1063/1.3159032

[17] H. Marinchio, C. Palermo, G. Sabatini, L. Varani, P. Shiktorov, E. Starikov, and V. Gružinskis, Pseudo-two-dimensional Poisson equation for the modeling of field-effect transistors, J. Comput. Electron. **9**(3–4), 141–145 (2010), https://doi.org/10.1007/s10825-010-0333-8

[18] S.-M. Hong and J.-H. Jang, Numerical simulation of plasma oscillation in 2-D electron gas using a periodic steady-state solver, IEEE Trans. Electron Dev. **62**(12), 4192–4198 (2015), https://doi.org/10.1109/TED.2015.2489220

[19] D. Scharfetter and H. Gummel, Large-signal analysis of a silicon Read diode oscillator, IEEE Trans. Electron Dev. **16**(1), 64–77 (1969), https://doi.org/10.1109/T-ED.1969.16566

[20] C. Jungemann, T. Linn, K. Bittner, and H.-G. Brachtendorf, Numerical investigation of plasma effects in silicon MOSFETs for THz-wave detection, Solid State Electron. **128**, 129–134 (2017), https://doi.org/10.1016/j.sse.2016.10.030

[21] G. Leuzzi and V. Stornelli, A frequency- and space-domain series-expansion approach for efficient numerical modeling of semiconductor devices, IEEE Trans. Electron Dev. **55**(12), 3525–3531 (2008), https://doi.org/10.1109/TED.2008.2006740

[22] S. Rudin, Temperature dependence of the nonlinear plasma resonance in gated two-dimensional semiconductor conduction channels, Appl. Phys. Lett. **96**(25), 252101 (2010), https://doi.org/10.1063/1.3455993

[23] S. Rudin, Non-linear plasma oscillations in semiconductor and graphene channels and application to the detection of terahertz signals, Int. J. High Speed Electron. Syst. **20**(03), 567–582 (2011), https://doi.org/10.1142/S0129156411006866

[24] S. Rudin, G. Rupper, A. Gutin, and M. Shur, Theory and measurement of plasmonic terahertz detector response to large signals, J. Appl. Phys. **115**(6), 064503 (2014), https://doi.org/10.1063/1.4862808

[25] G. Rupper, S. Rudin, and M. Shur, Response of plasmonic terahertz detectors to amplitude modulated signals, Solid State Electron. **111**, 76–79 (2015), https://doi.org/10.1016/j.sse.2015.05.035

[26] G. Rupper, S. Rudin, and F.J. Crowne, Effects of oblique wave propagation on the nonlinear plasma resonance in the two-dimensional

231   ISSN 1648-8504   eISSN 2424-3647

*J. Vyšniauskas et al. / Lith. J. Phys. **63**, 218–232 (2023)*

channel of the Dyakonov–Shur detector, Solid State Electron. **78**, 102–108 (2012), https://doi.org/10.1016/j.sse.2012.05.052

[27] S. Rudin and G. Rupper, Plasma instability and wave propagation in gate-controlled GaN conduction channels, Jpn. J. Appl. Phys. **52**(8S), 08JN25 (2013), https://doi.org/10.7567/JJAP.52.08JN25

[28] S. Rudin, G. Rupper, and M. Shur, Ultimate response time of high electron mobility transistors, J. Appl. Phys. **117**(17), 174502 (2015), https://doi.org/10.1063/1.4919706

[29] K.S. Kim, M.W. Ryu, J.S. Lee, and K.R. Kim, Accurate analysis and characterization of silicon field effect transistor-based terahertz wave detector with quasi-plasma two-dimensional electron gas, J. Nanosci. Nanotechnol. **16**(5), 4746–4752 (2016), https://doi.org/10.1166/jnn.2016.12241

[30] J. Vyšniauskas, A. Lisauskas, M. Bauer, D. Čibiraitė, J. Matukas, and H.G. Roskos, Hydrodynamic modelling of terahertz rectification in AlGaN/GaN high electron mobility transistors, J. Phys. Conf. Ser. **906**(1), 012023 (2017), https://doi.org/10.1088/1742-6596/906/1/012023

[31] Z.-Y. Liu, L.-Y. Liu, J. Yang, and N.-J. Wu, A CMOS fully integrated 860-GHz terahertz sensor, IEEE Trans. Terahertz Sci. Technol. **7**(4), 455–465 (2017), https://doi.org/10.1109/TTHZ.2017.2692040

[32] J. Delgado-Notario, J. Velazquez-Perez, Y. Meziani, and K. Fobelets, Sub-THz imaging using nonresonant HEMT detectors, Sensors **18**(2), 543 (2018), https://doi.org/10.3390/s18020543

[33] X. Liu and M. Shur, An efficient TCAD model for TeraFET detectors, in: *Proceedings of the 2019 IEEE Radio and Wireless Symposium (RWS)* (IEEE, Orlando, FL, USA, 2019) pp. 1–4, https://doi.org/10.1109/RWS.2019.8714400

[34] X. Liu and M.S. Shur, TCAD model for TeraFET detectors operating in a large dynamic range, IEEE Trans. Terahertz Sci. Technol. **10**(1), 15–20 (2020), https://doi.org/10.1109/TTHZ.2019.2952248

[35] T. Linn, Z. Kargar, and C. Jungemann, Investigation of moments-based transport models applied to plasma waves and the Dyakonov–Shur

instability, Semicond. Sci. Technol. **34**(1), 014002 (2019), https://doi.org/10.1088/1361-6641/aaf27a

[36] V. Gružinskis, P. Shiktorov, E. Starikov, H. Marinchio, C. Palermo, J. Torres, and L. Varani, Stepped current-voltage relation and THz oscillations in GaN MOSFET due to optical phonon emission: Monte Carlo simulation, J. Phys. Conf. Ser. **647**, 012034 (2015), https://doi.org/10.1088/1742-6596/647/1/012034

[37] C. Palermo, J. Torres, L. Varani, V. Gružinskis, E. Starikov, P. Shiktorov, S. Ašmontas, and A. Sužiedelis, Monte Carlo simulation of THz radiation detection in GaN MOSFET n^+nn^+ channel with uncentered gate in n-region, J. Phys. Conf. Ser. **906**, 012013 (2017), https://doi.org/10.1088/1742-6596/906/1/012013

[38] J. Mateos and T. Gonzalez, Plasma enhanced terahertz rectification and noise in InGaAs HEMTs, IEEE Trans. Terahertz Sci. Technol. **2**(5), 562–569 (2012), https://doi.org/10.1109/TTHZ.2012.2209970

[39] H. Lin, N. Goldsman, and I. Mayergoyz, Device modeling by deterministic self-consistent solution of Poisson and Boltzmann transport equations, Solid State Electron. **35**(6), 769–778 (1992), https://doi.org/10.1016/0038-1101(92)90277-J

[40] S.-M. Hong and C. Jungemann, A fully coupled scheme for a Boltzmann-Poisson equation solver based on a spherical harmonics expansion, J. Comput. Electron. **8**(3–4), 225–241 (2009), https://doi.org/10.1007/s10825-009-0294-y

[41] S.-M. Hong, G. Matz, and C. Jungemann, A deterministic Boltzmann equation solver based on a higher order spherical harmonics expansion with full-band effects, IEEE Trans. Electron Dev. **57**(10), 2390–2397 (2010), https://doi.org/10.1109/TED.2010. 2062519

[42] D. Ruić and C. Jungemann, Numerical aspects of noise simulation in MOSFETs by a Langevin–Boltzmann solver, J. Comput. Electron. **14**(1), 21–36 (2015), https://doi.org/10.1007/s10825-014-0642-4

[43] Z. Kargar, T. Linn, D. Ruic, and C. Jungemann, Investigation of transport modeling for plasma waves in THz devices, IEEE Trans. Electron

Dev. **63**(11), 4402–4408 (2016), https://doi.org/10.1109/TED.2016.2608422

[44]Z. Kargar, T. Linn, and C. Jungemann, Investigation of the Dyakonov–Shur instability for THz wave generation based on the Boltzmann transport equation, Semicond. Sci. Technol. **33**(10), 104001 (2018), https://doi.org/10.1088/1361-6641/aad956

[45]S. Cha and S.-M. Hong, Theoretical study of electron transport properties in GaN-based HEMTs using a deterministic multi-subband Boltzmann transport equation solver, IEEE Trans. Electron Dev. **66**(9), 3740–3747 (2019), https://doi.org/10.1109/TED.2019. 2926857

[46]P. Földesy, Terahertz responsivity of field-effect transistors under arbitrary biasing conditions, J. Appl. Phys. **114**(11), 114501 (2013), https://doi.org/10.1063/1.4821250

[47]S. Boppel, M. Ragauskas, A. Hajo, M. Bauer, A. Lisauskas, S. Chevtchenko, A. Rämer, I. Kašalynas, G. Valušis, H.J. Würfl, W. Heinrich, G. Tränkle, V. Krozer, and H.G. Roskos, 0.25-um GaN TeraFETs optimized as THz power detectors and intensity-gradient sensors, IEEE Trans. Terahertz Sci. Technol. **6**(2), 348–350 (2016), https://doi.org/10.1109/TTHZ.2016.2520202

[48]K. Ikamas, A. Lisauskas, S. Massabeau, M. Bauer, M. Burakevič, J. Vyšniauskas, D. Čibiraitė, V. Krozer, A. Rämer, S. Shevchenko, W. Heinrich, J. Tignon, S. Dhillon, J. Mangeney, and H.G. Roskos, Sub-picosecond pulsed THz FET detector characterization in plasmonic detection regime based on autocorrelation technique, Semicond. Sci. Technol. **33**(12), 124013 (2018), https://doi.org/10.1088/1361-6641/aae905

[49]M. Bauer, A. Rämer, S.A. Chevtchenko, K.Y. Osipov, D. Čibiraitė, S. Pralgauskaitė, K. Ikamas, A. Lisauskas, W. Heinrich, V. Krozer, and H.G. Roskos, A high-sensitivity AlGaN/GaN HEMT terahertz detector with integrated broadband bow-tie antenna, IEEE Trans. Terahertz Sci. Technol. **9**(4), 430–444 (2019), https://doi.org/10.1109/ TTHZ.2019.2917782

[50]Y. Zhu, Q. Ding, L. Xiang, J. Zhang, X. Li, L. Jin, Y. Shangguan, J. Sun, and H. Qin, 0.2–4.0 THz broadband terahertz detector based on antenna-coupled AlGaN/GaN HEMTs arrayed in a bow-tie pattern, Opt. Express **31**(6), 10720–10731 (2023), https://doi.org/10.1364/OE.483605

AlGaN/GaN TRANZISTORINIŲ THz DAŽNIŲ DETEKTORIŲ DVIMATIS HIDRODINAMINIS MODELIAVIMAS

J. Vyšniauskas [a], K. Ikamas [a, b], D. Vizbaras [a], A. Lisauskas [a]

[a] *Vilniaus universiteto Fizikos fakulteto Taikomosios elektrodinamikos ir telekomunikacijų institutas, Vilnius, Lietuva*

[b] *Generolo Jono Žemaičio Lietuvos karo akademijos Logistikos ir gynybos technologijų valdymo tyrimų grupė, Vilnius, Lietuva*

Santrauka

Pateikiami AlGaN/GaN didelio judrio lauko tranzistoriais paremtų terahercų dažnių juostos detektorių skaitmeninio modeliavimo rezultatai. Sprendimo būdas pagrįstas trijų Bolcmano pernašos lygties (BTE) momentų bei Puasono lygties sprendimu dvimatėje erdvėje. Tam tikslui buvo panaudota „Synopsys TCAD Sentaurus" programinė įranga. Joje įdiegta išsami medžiagų duomenų bazė bei suteiktos galimybės įskaityti pagavimo būsenas bei poliarizacijos reiškinį, ir tai leidžia suformuoti modelyje laidų kanalą nenaudojant legiravimo. Dažniausiai naudojamų modelių prielaidos buvo nagrinėjamos ir analitiškai, ir skaitmeniškai. Pateikiamos apskaičiuotos srovės jautrio $\mathfrak{R}_I$ verčių priklausomybės nuo santakos įtampos 0,01–3,0 THz dažnių ruože trims AlGaN sluoksnių storiams $d = 15, 20, 25$ nm ir skirtingiems užtūros ilgiams. Mes parodome, kad tik hidrodinaminis modelis gali atkurti srovės jautrumo ženklo pasikeitimą ties užtūros įtampa U_{G0} ($\mathfrak{R}_I = 0$ ties $U_G = U_{G0}$). Šį reiškinį nulemia energijos srauto koeficientas energijos balanso lygtyje. Modeliuotoms struktūroms gaunama ekvivalentinė triukšmo galia gali siekti $0,1\,\mathrm{pW}/\sqrt{\mathrm{Hz}}$ ties 0,04 THz ir $10\,\mathrm{pW}/\sqrt{\mathrm{Hz}}$ ties 3,0 THz.